ORIGINAL ARTICLE

Integrated Spectroscopic, Bio-active Prediction and Analytics of Isoquinoline Derivative for Breast Cancer Mitigation

Chioma G. Apebende[1,2] · Precious S. Idante[1,2] · Hitler Louis[1,2] · Umar S. Ameuru[3] · Tomsmith O. Unimuke[1,2] · Terkumbur E. Gber[1,2] · Ernest A. Agwamba[1] · Innocent Benjamin[1] · Fredrick C. Asogwa[1,2]

Abstract

Breast cancer has been declared as the world's most prevalent cancer with over 7.8 million fatalities reported in 2020. Despite the numerous efforts in therapeutics and early detection programmes in combination with several treatment, the rate of mortality reported is still on the increase. This might arise from the insufficient data recorded in terms of healthcare analytics of the therapeutic agents used along with patients' responsiveness and health complications. Thus, the need for the development, optimization and screening of more efficient bioactive therapeutic targets. Herein, we report the synthesis, spectroscopy and in-silico analysis of (E)-2-decyl-6-((6,7-dihydroxynaphthalen-1-yl)diazinyl)-1H-[de] isoquinoline-1,3(2H)-dione (**AGI**) as potential bioactive anti-cancer agent. Koopman's approximation method was utilized for the analysis of global reactivity and stability parameters of the considered structure. The studied structure was observed to have an energy gap of 2.806 eV. Several population analyses, frontier molecular orbitals, and non-linear optical (NLO) analysis were computed at the same theoretical level. The anticancer potency of the studied structure was further assessed via in-silico molecular docking. From the docking analysis, higher binding affinity were observed to be −9.90 kcal/mol and −10.10 kcal/mol for **AGI** and ARO interaction with 4R5Y amino acid. The conventional therapeutic candidate (Aromasin) for breast cancer was used as standard reference to appraise the efficacy of the studied structure. The findings of this study affirm the potential utilization of the studied system in the formulation and mitigation of breast cancer. The methods used to arrive at these conclusions are accurate and predict the various properties to reasonable extent.

Keywords Breast cancer · Koopmans method · Spectroscopic method · Molecular docking method

1 Introduction

The lining cells (epithelium) of the ducts (85%) or lobules (15%) in the glandular tissue of the breast are where breast cancer begins to develop. The malignant development is initially contained within the duct or lobule ("in situ"), where it often exhibits no symptoms and has a low risk of spreading (metastasis). These in situ (stage 0) tumors may develop over time and infect the breast tissue around them (invasive breast cancer), then disseminate to neighboring lymph nodes (regional metastasis), or to other body organs (distant metastasis). Widespread metastases are the cause of breast cancer deaths in women. One of the main issues with public health is cancer (particularly breast cancer). According to the World Health Organization (WHO), it is really the second most common cause of high mortality rates worldwide, accounting for 685,000 fatalities in 2020 [1]. Standard breast cancer treatments including chemotherapy, surgery, and radiotherapy don't work very well and frequently have side effects like nausea, bone marrow failure, and the emergence of drug resistance (MDR) [2]. Discovering a novel therapeutic modality that will completely eradicate cancer tumors without causing any adverse effects is so imperative. As a result of their interactions with the active sites of proteins, isoquinoline derivatives have been shown in studies to inhibit dinuclear ribonucleic acid

✉ Chioma G. Apebende
gloriaapebende@yahoo.com

✉ Hitler Louis
louismuzong@gmail.com

1 Computational and Bio-Simulation Research Group, University of Calabar, Calabar, Nigeria

2 Department of Pure and Applied Chemistry, Faculty of Physical Sciences, University of Calabar, Calabar, Nigeria

3 Department of Polymer and Textile Engineering, Ahmadu Bello University Zaria, Zaria, Nigeria

(DNA), ribonucleic acid (RNA), carcinogenesis, and protein synthesis. This is because they contain the (–N=N–) in their molecular structures [3]. Further studies also revealed that isoquinoline compounds manifest cytotoxic actions against Ehrich liter ascites carcinoma (EAC), epithelial cell line (MCF-7) and (MDA-MB-231) obtained from breast cancer, PC-3 human prostate cancer (PC-3) and myelogenous leukemia tumor cells (K562) [4].

Herein, the structural analytics and synthesis of **AGI** is reported. The studied compound was synthesized and characterized using proton (^{1}H-NMR) and carbon (^{13}C-NMR) nuclear magnetic resonance spectroscopy as well as the Fourier transformer infrared (FTIR) and Mass spectroscopic techniques. The structure was further confirmed by considering the theoretical spectroscopic assignments of vibrational frequencies as well as the proton NMR and ultraviolet visible spectroscopy via the time dependent density functional theory analytical approach. The simulated spectra using DFT calculations could be used to support the experimental spectra analysis. Density functional theory (DFT) was used in conjunction with the 6-31G* basis set and the hybrid functional of Becke's 3 Lee-Yang–Parr parameters (B3LYP) to perform computational quantum simulations. The models were successful in foreseeing the compatibility between the studied compound's geometric and electrical properties [5]. Global reactivity and molecular characteristics like the frontier molecular orbital and stability descriptors were analyzed by utilizing the Koopmans' approximation. The nonlinear optical properties of the considered structure were equally assessed via the first order hyperpolarizability index. To understand the molecular hybridization, resonance, donor–acceptor interactions and stability of the compound, natural bond orbital analysis was computed to this effect [6]. Four population analysis based on Mulliken population, Natural population, atomic dipole moment corrected Hirshfeld population (ADCH) and Charges from electrostatic potentials using a Grid-based method (CHELPG) were compared to scrutinized the most reactive sites in the compound. The pharmacological analytics of the considered structure was further evaluated in-silico via the Swiss adsorption, distribution, metabolism and excretion predictor as well as the PKCSM online predictor [7]. Moreover, molecular docking simulations have been considered by utilizing the Lamarckian search algorithm for the detection of the anti-cancer potency of the compound in comparison to conventional therapeutic agent (Aromasin).

2 Materials and Methods

The experimental methods and analysis of the synthesized compound have been reported in our previous work by Eno et al. [8]. However, the procedure for the synthesis of the studied dye and the synthetic route is given in Scheme 1.

2.1 Procedure for the Synthesis of the Studied Dye

(E)-2-decyl-6-((6,7-dihydroxynaphthalen-1-yl) diazinyl)-1H-[de] isoquinoline -1,3(2H)-dione (AGI) At temperatures below 10 °C, sodium nitrite (1.5 mmol, 0.104 g) was gently added with steady stirring to cold concentrated sulphuric acid (98%, 1.1 mL). Using a water bath, the temperature of the reaction mixture was progressively raised to 65 °C until all of the sodium nitrite had dissolved. The solution was then externally cooled to 5 °C and diluted using a propionic acid/glacial acetic acid combination (10 mL, 1.5:8.5 volume ratio) Below 10 °C, a fraction of finely ground powder of 4-amino-*N*-dodecyl-1,8-naphthalimide (1.5 mmol) was added and the mixture was agitated for 3 h. The transparent diazonium salt solution was immediately employed in coupling reactions with 2-naphthol (1.5 mmol) dissolved in ethanol by adding it over 30–40 min while vigorously stirring. The mixture was agitated for another 2 h at 5 °C. Using 10% sodium acetate, the pH of the solution was adjusted to 4–5 and agitated for 1 h. The final product was then filtered, rinsed with warm water, then cold water, and dried. The crude product was refined multiple times by recrystallization from DMSO to get AGI (yield 80.9%). The residual DMSO was removed from the result by repeatedly washing the precipitate with water and aqueous ethanol (50%) [20].

2.2 Computational Method of Analysis

The geometrical structure of the studied compound (*E*)-2-decyl-6-((6,7-dihydroxynaphthalen-1-yl) diazinyl)-1H-[de] isoquinoline-1,3(2H)-dione **(AGI)** was optimized using electronic structure theory technique based on density functional theory (DFT) with the B3LYP functional and the 6-31G* basis set utilizing Gaussian 09 W [9] and Gaussview 6.0.16 software [10]. Koopmans' approximation for the determination of global descriptors such as chemical softness, hardness, electrophilicity index, ionization potential and electron affinity were utilized as appropriate. Natural bond orbital (NBO) analyses, non-linear optics (NLO), Natural population analysis (NPA) and Mulliken population analysis (MPA) were calculated by DFT method at the CAM-B3LYP/6-31G(d) level using the Gaussian software. The Coulomb attenuated functional (CAM-B3LYP) provides the best overall performance in terms of excited state calculations, hence its utilization. More so, Time dependent-density functional theory (TD-DFT) method at the B3LYP/6-31G(d) level was used for the computations of the UV–Vis spectrum. Proton nuclear magnetic resonance spectrum (^{1}H-NMR) was calculated using the Gauge-invariant atomic orbital (GIAO) model.
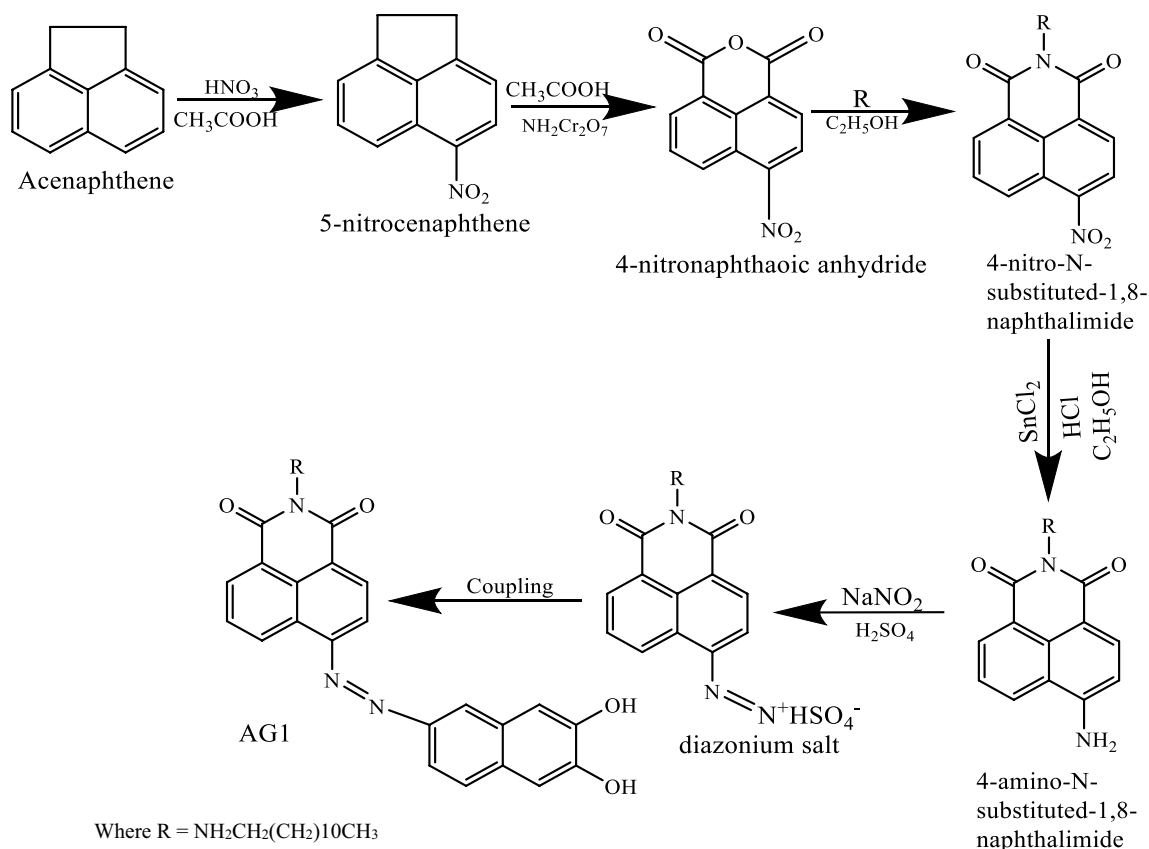
Scheme 1 Synthetic route of **AGI**

The Fourier transform infrared (FTIR) spectrum was computed using Gaussian 09 W and Gaussview 6.0 software by performing frequency calculations and the analysis obtained by the Vibrational energy distribution analysis (VEDA4) programme on the basis of their potential energy distribution (PED) assignments [11]. The various population analysis and atomic densities of state were computed with the aid of multiwfn software [12]. The oral bioavailability and pharmacological analysis were obtained by the Swiss adsorption, distribution, metabolism and excretion online predictor as well as the PKCSM server. Auto dock Vina, discovery studio visualizer and Molegro virtual docker were employed to perform molecular docking analysis. Cancerous proteins with designated protein data bank codes: (5T1Z, 5T7F, 4R5Y, 4JT6 and 20VM) were selected as targets for detecting the anti-cancer efficacy of the studied compound. Aromasin was chosen as the standard for comparison.

3 Results and Discussion

3.1 Spectroscopic Analysis

3.1.1 Vibrational Analysis

Infrared spectroscopy helps ensure regulatory compliance through validation protocols, it has been widely used in pharmaceutical, plastics and polymer industry amongst others because of its high sensitivity, simplicity and fastness [13]. **AGI** was observed to have a 3n-6 modes of vibrations where n represents the number of atoms. With $n = 72$ atoms, the compound has 210 vibrational modes out of which 71 were stretching (49 symmetric and 22 asymmetric stretch), 70 In plane bending (44 symmetric and 26 asymmetric bend), 56 torsional (37 symmetric and 19 asymmetric tor) and 13 out of plane bending (7 symmetric

Table 1 Experimental and theoretical vibrational energy distributional analysis of the synthesized compound (**AGI**)

Experimental wave number (cm^{-1}) unscaled	Theoretical wave number (cm^{-1}) scaled	PED assignment (%)	Raman activity
3375	3625	$_{\upsilon}$OH(100)	2.2304
3063	3067	$_{Asy\upsilon}$CH(82)	2.6607
2921	2940	$_{Asy\upsilon}$CH(91)	7.5811
1699	1697	$_{Asy\upsilon}$OC(83)	4.9258
1658	1648	$_{Asy\upsilon}$CC(52) + $_{\upsilon}$CC(11)	7.0624
1618	1624	$_{Asy\upsilon}$CC(45)	15.2705
1588	1576	$_{\beta}$HOC(19)	34.0269
1382	1391	$_{\upsilon}$CC(40)	38.9449

and 6 asymmetric out of plane) vibrations. The experimental and theoretical results with the potential energy distribution (PED) assignments of the investigated compound **AGI** are presented in Table 1.

However, full detail of the FTIR theoretical result could be seen in Table S3 of the supporting document. Also, all the spectral are provided in the manuscript supporting information.

C–H vibrations

According to reported works in literature [14], the C–H stretching vibrations range between 3000 and 2840 cm^{-1} for alkane, 3100–3050 cm^{-1} for alkene, 3050–3000 cm^{-1} for arene and alkyne is expected around 3300 cm^{-1}. Asymmetric stretching vibration between C and H (of C–H bond) that is related to the CH3 group on the alkyl chain of the compound. However, in this study C–H stretching was experimentally observed at 3063 and 2921 cm^{-1} and theoretically estimated at 3067 and 2940 cm^{-1} with a PED contribution of 82 and 91%.

O–H vibrations

Within the IR region, between 3650 and 3600 cm^{-1} [15], a sharp absorption peak is connected to the free O–H stretch. When alcohol is dissolved in a solvent, this manifests with an O–H peak that is hydrogen-bonded. The O–H stretching vibration of **AGI** was experimentally observed to have a wave number of 3375 cm^{-1} and theoretically estimated at 3625 cm^{-1} as clearly shown by Table 7 with a PED contribution of 100%.

C=C vibrations

Aromatic rings C=C usually appear between 1600 and 1450 cm^{-1} region [16] with weak overtone bands at 2000–1667 cm^{-1} used for the assignment of substitution on aromatic rings. The aromatic C=C experimental stretching vibration of **AGI** was observed at 1699, 1658 and 1618 cm^{-1}. However, the theoretical values were computed at 1695, 1648 and 1624 cm^{-1} with PED assignments of 65, 52% for asymmetric and 11% for symmetric C=C and 45% contributions respectively. This could be due to conjugation effect which increases the single bond character of the C=O and C=C bonds in the resonance hybrid thereby, causing

the lowering of the force constant and the corresponding frequency. More so, the stretching vibration experimentally observed at 1382 cm^{-1} and theoretically computed at 1391 cm^{-1} with a PED contribution of 40% could be attributed to C–C single bond symmetric stretching vibrations.

C–O–H vibrations

C–O–H bending vibrations generally appears as a weak and broad absorption band around 1440 to 1220 cm^{-1} region [17]. The structure under study was observed to experimentally have a C–O–H bending vibration at 1382 cm^{-1} and theoretically estimated at 1391 cm^{-1} with a PED contribution of 19%. The FTIR data collated for both experimental and theoretical studies are observed to be in perfect agreement and could therefore be inferred that the theoretical study is a perfect validation of the experimental work. Lastly, information on the geometrical parameters of the compound could be found in Table S4 of the supporting documents.

3.1.2 ^{1}H-NMR Analysis

The experimental investigation of **AGI** ^{1}H-NMR was logged in deuterated chloroform (CDCl$_3$) as the standard solvent. The theoretical ^{1}H-NMR was carried out using cathode-like polarizable continuum model (CPCM) in chloroform as the solvent with CAM-B3LYP/ 6-31G(d) basis set by the Gauge-invariant atomic orbital (GIAO) method [18] and tetramethylsilane (TMS HF/6-31G(d) GIAO) as the internal standard. The theoretical and practical ^{1}H-NMR chemical shift values reported in parts per million (ppm) and the corresponding assignments are shown in Table 2

The chemical shift values of 0.88 and 0.85 ppm recorded for the experimental and theoretical work, is evidence of the presence of –CH$_3$ protons (H$_{53}$) at some distance from electronegative atoms in **AGI**. The experimental and theoretical chemical shift values computed at 1.26–1.74 ppm and 1.34–1.76 ppm (triplet, H$_{46}$–H$_{29}$) indicates –CH$_2$ protons of alkyl chain in the studied compound. Most interestingly, is the both theoretical and experimental chemical shift values of some multiplets observed at 4.03 and 4.07 ppm (H$_{25}$) which is due to –NH protons of aromatic rings in **AGI.** The

Table 2 Comparison of the experimental and theoretical ^{1}H-NMR result of **AGI**

S/no.	Experimental (ppm)	Theoretical (ppm)	Assignment
1	0.88	0.85	Singlet, $-CH_3$ protons at some distance from electronegative atoms (H_{53})
2	1.26–1.74	1.34–1.76	Triplet, $-CH_2$ protons of the alkyl chain (H_{46}–H_{29})
3	4.03	4.07	Multiplet, $-CH$ protons of aromatic ring (H_{25})
4	6.52	6.39	Triplet, $-CH$ protons of aromatic ring (H_{67})
5	7.26–7.41	7.20	Doublet, $-CH$ protons of aromatic ring (H_{65})
6	7.49	7.45	Multiplet, $-CH$ protons of aromatic ring (H_{68})
7	7.65	7.64	Doublet, $-CH$ protons of aromatic ring (H_{15})
8	7.99	7.98	Multiplet, $-CH$ protons of aromatic ring (H_{60})
9	8.20	8.19	Doublet, $-CH$ protons of aromatic ring (H_8)
10	8.40	8.49	Triplet, $-CH$ protons of aromatic ring (H_{62})
11	16.67	16.65	Doublet $-OH$ proton of the aromatic ring (H_{70})

presence of –CH protons directly attached to the aromatic ring is observed at 6.52 and 6.39 ppm (H_{67}) for the experimental and hypothetical values. More so, the observed theoretical chemical shift values of H_{65}, H_{68}, H_{15}, H_{60}, H_8 and H_{62} at 7.20, 7.45, 7.64, 7.98, 8.19 and 8.49 ppm are in perfect agreement with the experimental chemical shift values at 7.26–7.41, 7.49, 7.65, 7.99, 8.20 and 8.40 ppm which indicates -CH protons of aromatic ring. Nevertheless, the experimental chemical shift value at 16.67 ppm could not be theoretically validated. This could be attributed to the high deshielding level and extremely downfield position of the proton(s) at the said region. We therefore conclude that, the major protons which caused the observed chemical shift values are those of, –CH$_3$, –CH$_2$, –NH of aromatic rings and –CH of aromatic rings in AGI. Figure S2a and S2b of the supporting document show the experimental and theoretical ^{1}H NMR spectrum of AGI.

3.1.3 UV–Vis Spectroscopic Analysis

To comprehend and clearly explain the different kinds of electronic excitation (rotational and vibrational modes) in the investigated compound, UV–Vis spectroscopic study

has been obtained using the CAM-B3LYP/6-31G(d) basis set and the TD-DFT approach, due to the fact that CAM-B3LYP offers the best result in an excited state calculation [19].

Table 3 shows the experimental and theoretical results for oscillator strength (f value), energy of excitation (E), percent contribution, and potential assignments carried out in four (4) different solutions (DMF, CHCl$_3$, EtOH and EtOH + HCl) for the experimental and gas phase. From the Table 3, the result showed that all phases of orbital 136–140 exhibit an excited state transition from S0 to S1 with an assignment of $n \rightarrow \pi$ (non-bonding orbital to the—antibonding orbital). Additionally, the wavelength (max) values for the theoretical and actual phases indicate that the electronic excitation of AGI mostly took place in the visible spectrum. The experimental result showed the highest absorption wavelength of 515 nm in DMF and CHCl$_3$ phases while lower wavelengths (512 nm) of absorption were observed in other solvents which is attributed to the presence of OH group in these phases thus, causing a hypsochromic or blue shift in **AGI** [20]. Inference could therefore be made that the absorptivity of the studied compound with respect to solvation follows the order: DMF=CHCl$_3$ > EtOH=EtOH + HCl.

Table 3 UV–Vis spectroscopy of the experimental and theoretical values of **AGI** using the CAM-B3LYP/6-31G(d) basis set and the TD-DFT method

Phase	Experimental wave length (nm)	Phase	Theoretical wave length (nm)	Excited state	Energy	f value	% contribution	Assignment
DMF	515	Gas	499.71	S_0–S_1 136–140	2.4811 eV	0.0498	0.4960	$n \rightarrow \pi^*$
CHCl$_3$	515	CHCl$_3$	502.57	S_0–S_1 136–140	2.4670 eV	0.0902	1.6272	$n \rightarrow \pi^*$
EtOH	512	EtOH	502.39	S_0–S_1 136–140	2.4679 eV	0.0881	1.5523	$n \rightarrow \pi^*$
EtOH + HCl	512	H$_2$O	502.42	S_0–S_1 136–140	2.4677 eV	0.0889	1.5806	$n \rightarrow \pi^*$

On the other hand, the theoretical studies showed the highest absorption wavelength (λ_{max}) of 502.57 nm in CHCl$_3$ phase with excitation energy of 2.4670 eV, oscillator strength of 0.0902 and a contribution of 1.63% whose assignment corresponds to that of the non-bonding to pi-antibonding orbital transition. The interaction between the heteroatom orbital and the π-antibonding orbital of the studied compound might likely be the cause. However, the lowest wavelength (λ_{max}) of 499.71 nm was seen in gas phase with an excitation energy of 2.4811 eV, contribution of 0.4960%, ocillator strength of 0.0498, and an assignment of n → π*. Further analysis of the result showed that the absorption wavelength inversely correlated with excitation energy. Nevertheless, the theoretical results in all phases are in accordance with the experimental values which suggest an absorption in the visible region of the electromagnetic spectrum thus **AGI** possesses substantial fluorescing property.

3.2 Frontier Molecular Orbital (FMO) Analysis

The highest occupied molecular orbital (HOMO) and lowest unoccupied molecular orbital (LUMO) were utilized as a measure for assessing the chemical and electronic reactivity of the studied compound [21] HOMO–LUMO, and Energy gap of the studied compound is shown in Fig. 1

As shown in Fig. 1, the density of the HOMO is primarily localized on the naphthalene ring and partially on the isoquinoline ring with a value of − 5.716 eV. However, the LUMO electron density, which has a value of − 2.910 eV, is shown to be completely localized on all the aromatic ring atoms, including the N-atoms. Further investigations made as to vividly explain the specific orbitals in which the HOMO and LUMO reside showed that HOMO (orbital 139), is on N22, C54, C55, C59, C61, C64 and O69 while the LUMO (orbital 140) resides on C2, C6, C17, C55, O19, N21 and N22 atoms, respectively. This suggests a donor – acceptor electron movement after energy absorption [22]. Furthermore, the HOMO–LUMO energy gap which corresponds to the difference between HOMO and LUMO energies of the studied compound is theoretically found to be at a value of 2.80 6 eV. This accounts for the less stability and high chemical reactivity of the compound [23]. Global descriptors such as ionization energy (I), electron affinity (A), electronegativity (χ), electrochemical potential (μ), hardness (η), softness (S) and electrophilicity index (ω) were computed using Koopman's approximation as shown in Table 4. The equations are written as;
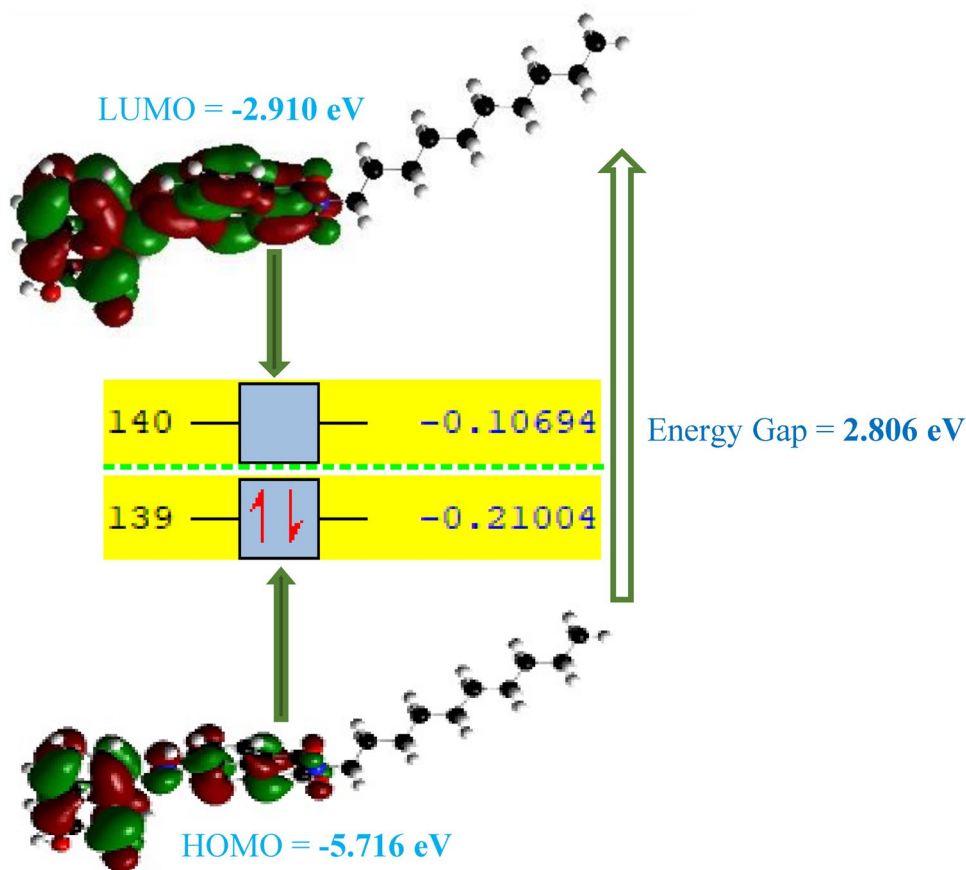
$$I = -\varepsilon_{HOMO} \tag{1}$$

Fig. 1 HOMO–LUMO

LUMO = **-2.910 eV**

140 — ☐ — -0.10694

139 — ⇅ — -0.21004

Energy Gap = **2.806 eV**

HOMO = **-5.716 eV**

Table 4 Global descriptors of the studied compound

Global descriptors	Value (eV)	Global descriptors	Value (eV)
HOMO	− 5.716	Electrochemical potential	− 2.910
LUMO	− 2.910	Hardness	1.403
Energy gap	2.806	Softness	0.701
Ionization energy	5.716	Electrophilicity	5.939
Electron affinity	2.910	Dipole moment	8.317
Electronegativity	4.313	Total energy	− 46,380.556

$$A = -\varepsilon_{LUMO} \tag{2}$$

The degree of stability that a system experiences when additional charges from the environment flow into the system is known as the electrophilicity index [24]. Hence, the electrophilicity index of the studied compound with a value of 5.939 eV indicates a high flow of electrons during donor–acceptor interaction. More so, the chemical hardness agrees with those reported in the literature and is directly connected with the reactivity and stability of the studied compound [25]. Finally, the electrochemical potential of the compound is a determinant of the outflow of electrons from the molecule.

3.3 Natural Bond Orbital (NBO) Analysis

NBO is used to determine resonance structure contributions to molecules and consequently, with the assistance of bonding and antibonding orbital interactions offers an effective method to understand the delocalization of electron density within molecules as well as intra- and intermolecular charge transfer interactions [26]. The second order energy is used to anticipate the strength of the delocalization interactions (stabilization energy) for each donor NBO (i) and acceptor NBO (j) and $E^{(2)}$ associated with electron delocalization between the donor and acceptor as shown in Eq. (3) [27].

$$E^{(2)} = n_r \frac{(F(i,j))^2}{E(j) - E(i)} \tag{3}$$

where $E(j) - E(i)$ is the difference in orbital energies of the donor and acceptor NBO orbitals, n is the population of the donor orbital, F_{ij} is the off-diagonal Fock matrix element. The predicted occupancies of natural orbitals (Lewis and Non-Lewis type and—bonded orbitals) are displayed in Tables S2a and S2b of the supplemental information. From the Tables 5, it is observed that π(N21–N22) bond have the least occupancy of 0.1963e which is formed from a hybrid of $SP^{99.99}$ on nitrogen 22 (99.58%, P character) interacting with π(C54–C56) formed from a hybrid of $SP^{1.00}$ (99.98% P-character). π(C9–C13) bond with occupancy of 0.2350 e which is

Table 5 Hybrid of **AGI** and natural orbital occupancies calculated by CAM-B3LYP method and 6-31G(d) functional

Donor Lewis– type NBOs	Occupancy	Hybridization	% atomic orbital
π$C9$–C_{13}	1.71225	$sp^{1.00}$	s(0.00%) p(99.94%) d(0.06%)
LP (1) N_{18}	1.62227	$sp^{99.99}d^{0.46}$	s(0.03%) p(99.95%) d(0.02%)
LP (2) O_{69}	1.86780	$sp^{1.00}$	s(0.00%) p(99.87%) d(0.13%)
LP (2) O_{71}	1.89465	$sp^{1.00}$	s(0.00%) p(99.90%) d(0.10%)
πC_3–C_4	0.44610	$sp^{1.00}$	s(0.00%) p(99.99%) d(0.01%)
πC_{16}–O_{19}	0.26602	$sp^{1.00}$	s(0.00%) p(99.81%) d(0.19%)
πC_{17}–O_{20}	0.26789	$sp^{1.00}$	s(0.00%) p(99.81%) d(0.19%)
πN_{21}–N_{22}	0.19638	$sp^{99.99}d^{1.92}$	s(0.14%) p(99.58%) d(0.27%)
πC_{55}–C_{58}	0.46752	$sp^{1.00}$	s(0.00%) p(99.98%) d(0.02%)
πC_{63}–C_{66}	0.30953	$sp^{1.00}$	s(0.00%) p(99.94%) d(0.06%)

formed from a hybrid of $SP^{1.00}$ on Carbon 13 (99.94% P-character) is observed to interact with π(C10–C12) forming a hybrid of $SP^{1.00}$ with 99.98% P-character. The bond between σ(C66–O71), has the highest occupancy of 1.99496e formed from a hybrid of $SP^{3.12}$ on oxygen 71 (75.57% P-character) interacting with LP (1) N18 with $SP^{99.99}$ hybrid (99.95% P-character. Also, σ(C17–N18) show a high occupancy of 1.99440 e formed from a hybrid of $SP^{2.09}$ on nitrogen 18 (67.57% P-character). In order to examine potential interactions between all of the bonding NBOs (Lewis or donors) and the antibonding (non-Lewis or acceptors), the second order perturbation theory is used. According to table S2b of the supporting information, for each donor (i) the higher the perturbation energy value, the stronger the interactions between the electron donors and acceptors, and the more intensely conjugated the system will be. Table 5 displays the most important intramolecular resonance interactions that lead to the maximum stabilization energy seen in the investigated molecule. For the NBO study of AG1, the important interactions and the value of their stabilization energies were as follows π(C55–C58) → π(C54–C56) 316.15 kcal/mol, π(C3–C4) → π(C1–C2) 309.08 kcal/mol, π(C63–C66) → π(C57–C61) 242.54 kcal/mol, π(C17–O20) → π(C5–C6) 155.87 kcal/mol, π(C16–O19) → π(C10–C12) 124.94 kcal/mol, LP(1) N18 → π(C17–O20) 67.03 kcal/mol, π(N21–N22) → π(C54–C56) 41.03 kcal/mol, LP(2) O69 → π(C57–C61) 37.46 kcal/mol,

Table 6 Second order perturbation theory analysis of **AGI** using CAM—B3LYP method and 6-31G(d) functional

Donor (i)	Occupancy	Acceptor (j)	Occupancy	E^2(kcal/ mol)	$E(j) - E(i)$ (a.u)	$F(i, j)$/a.u
πC_9–C_{13}	1.71225	πC_{10}–C_{12}	1.97384	29.68	0.38	0.095
$LP(1)N_{18}$	1.62227	πC_{17}–O_{20}	1.98961	67.03	0.35	0.141
$LP(2)O_{69}$	1.86780	πC_{57}–C_{61}	1.95252	37.46	0.45	0.122
$LP(2)O_{71}$	1.89465	πC_{63}–C_{66}	1.97766	32.47	0.47	0.117
πC_3–C_4	0.44610	πC_1–C_2	0.29147	309.08	0.01	0.088
πC_{16}–O_{19}	0.26602	πC_{10}–C_{12}	0.06188	124.94	0.02	0.082
πC_{17}–O_{20}	0.26789	πC_5–C_6	0.08326	155.87	0.02	0.083
πN_{21}–N_{22}	0.19638	πC_{54}–C_{56}	0.02578	41.03	0.05	0.079
πC_{55}–C_{58}	0.46752	πC_{54}–C_{56}	0.01946	316.15	0.01	0.088
πC^{63}–C_{66}	0.30953	πC_{57}–C_{61}	0.04228	242.54	0.01	0.089

Fig. 2 AGI atomic labelling
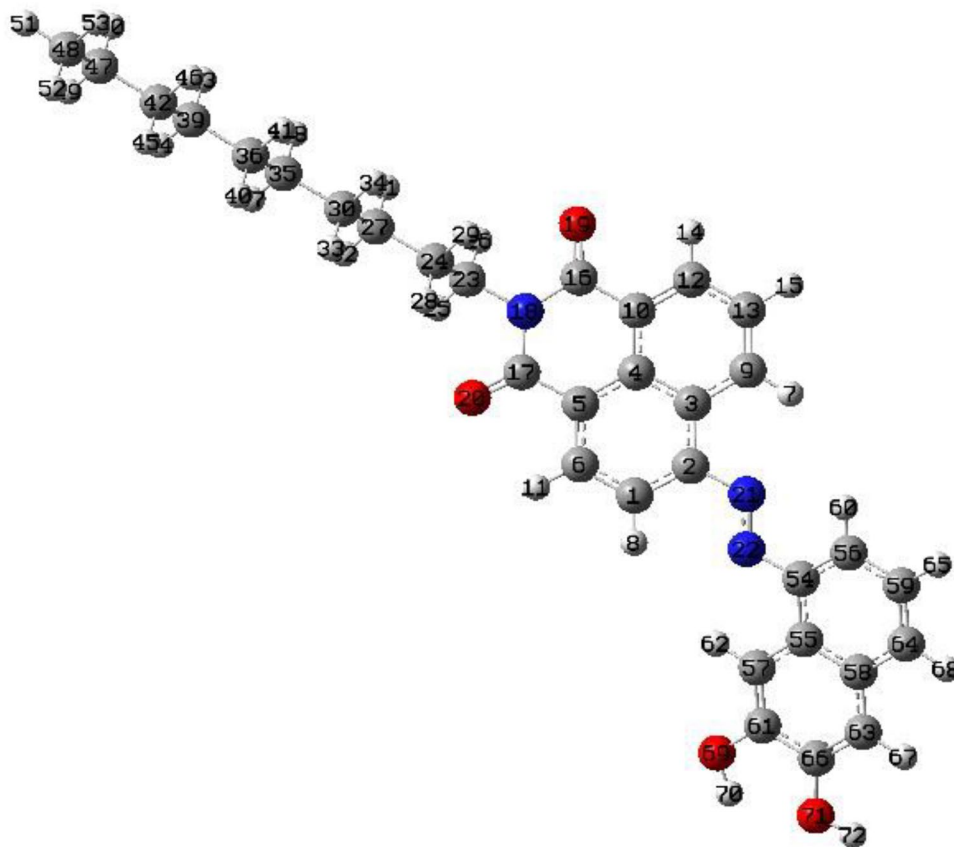
LP(2) O71 → π(C63–C66) 32.47 kcal/mol and π(C9–C13) → π(C10–C12) 29.68 kcal/mol. These strong interactions within the ring system as observed in Table 6. suggest an intense delocalized structure thus, an extra stability for AGI is due to resonance stabilization (Fig. 2).

3.4 Atomic Charge Analysis

Atomic charge is one of the most crucial ideas in chemistry. It offers a clear illustration of the dispersion of electron densities within molecules [27]. Atomic charges are very

crucial in understanding the relationship between a molecule's structural properties. Atomic charges can be calculated in a variety of methods, each with a distinct function. The Atomic Dipole Moment Corrected Hirshfeld (ADCH), Charges from Electrostatic Potentials using a Grid-Based method (CHELPG), Mulliken Population Analysis (MPA), and Natural Population Analysis (NPA) methods were used to determine the atomic charges of the target molecule, as shown in Table S5 of the supporting materials. The NPA and MPA are sensitive to basis set changes, which result in changes to the estimated net charges. NPA provides a

better charge distribution, since its calculation is based on the natural charge [28]. CHELPG charges are fitted to reproduce charges at a number of points around the molecule [29, 30] and so are not very suitable for the treatment of large systems where some of the innermost atoms are located far away from the points at which the molecular electrostatic potential is computed. Charges predicted from ADCH are very efficient and insensitive to basis set. However, the predicted charges are usually smaller than that of mulliken. Comparing the charges obtained using the various charge population methods listed above, the results showed that charge values for all the heteroatoms (oxygen and nitrogen) are negative for all the methods of calculations used in the sequence ADCH < CHELPG < MPA < NPA with the negative charge value of oxygen higher than nitrogen. This observation may be due to the high electronegativity of oxygen compare to nitrogen. Also, the charge values for all the hydrogen atoms are positive across all the population methods used except for some negligible few exceptions noticed in CHELPG values of H_{28}, H_{29}, H_{31}, H_{32}, H_{33}, H_{34}, H_{37}, H_{38}, H_{40}, H_{41}, H_{43}, H_{45}, H_{46}, H_{49} and H_{50} where the charge values are slightly negative. The positive charge values on hydrogen may be due to the fact that the surrounding atoms of hydrogen in the studied compound are higher in electronegative values than hydrogen. Also, the electron-donating effect of the two hydroxyl groups attached to the naphthalene ring may be responsible for slight negative charge on the above listed hydrogen. The carbon atoms in the **AGI** base on their positions have a diverse positive and negative charges for all the population analysis methods used with carbon 16 (C_{16}) having the highest positive charge of 0.71306 e and carbon 48 (C_{48}) having the highest negative charge of −0.68015 e both from NPA charges. The overall result is in line with the work done by Jebaraj et al. [31] and Obu et al. [32]. The charges are represented as a plot in Fig. 3.
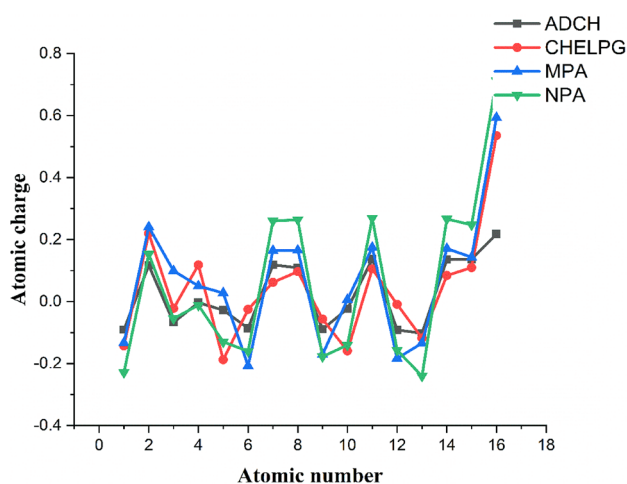

Fig. 3 Atomic charge plot

3.5 Non-linear Optics Analysis

Non-linear optical activity is produced as a result of the interaction between a laser beam and a material (organic nonlinear molecules) with emerging photonic technologies. When an applied electric field is present, this phenomenon takes place. Donor–acceptor interactions change the charge distribution in a molecule prior to excitation, and conjugation improves the dispersion of electrons even more [33]. However, the first order hyperpolarizability cannot be completely described without consideration of intramolecular charge transfer as electron clouds flow across a—conjugated system from the electron donor phase to the acceptor phase. NLO application could be felt in CARS microscopy where it is employed for various biological and pharmaceutical samples. NLO calculation of **AGI** was achieved by DFT method at CAM—B3LYP/6-31G(d) basis set in gas phase. The reference molecule (Urea) was optimized at the same level of theory. Furthermore, computation of non-linear optical properties such as Dipole moment (μ), Anisotropy of the polarizability (Δα), maximum value of dipole moment ($μ_z$), etc. were carried out using Multiwfn software with the aid of the.LOG file. Using the x, y, z components of these parameters [34] The highest value of dipole moment is observed in $μ_z$ (0.503 D) which is the maximum value of the dipole moment along the z axis. In this study, the values of $α_{total}$, $Δ_α$ and $β_{total}$ are converted from atomic units (a.u) to electronic units (esu) (for α, $1 a.u = 0.1482 \times 10^{-24}$ esu and for β, $1 a.u = 8.6393 \times 10^{-33}$ esu). The dipole moment and mean first hyperpolarizability values of the studied compound were theoretically calculated at 2.153 D and 7.289×10^{-30} esu as against the reference (Urea) which is computed at 1.3732 D and 0.3728×10^{-30} esu. Also observed, are the values of the mean polarizability or total polarizability and the anisotropy of the polarizability at 6.412×10^{-23} and 4.851×10^{-23} esu. This result implies that the total dipole moment of the studied compound is 1.57 times greater than the reference. Also, the value of 7.289×10^{-30} esu for AGI signifies that the studied compound is 19.6 times greater than the value of urea and therefore, suggests a better nonlinear optical activity in the studied compound compare to the reference compound and therefore, will exhibit excellent selectivity and reactivity property as evidenced in the docked result in Table 10. The NLO result is shown in Table 7.

3.6 Fragment Density of States (DOS)

To provide a more thorough explanation of the compound's electronic characteristics, total, overlap, and partial densities of states (TDOS, OPDOS, and PDOS) Calculations were made [35]. To analyze the nature and structure of electrons, however, the graphs produced by DOS are essential tools. The visual analysis of orbital composition heavily relies

Table 7 Non-linear optical properties of **AGI** calculated using CAM-B3LYP method, 6-31G(d) basis set and Multiwfn software

Dipole moment	Value (D)	Static polarizability	Value (a.u)	Static first hyper polarizability	Value (a.u)
X	0.461	αXX	391.335	βXXX	− 557.486
Y	− 3.117	αXY	19.528	βXXY	− 188.179
Z	0.503	αYY	692.873	βXYY	− 164.533
μ	2.153	αXZ	50.562	βYYY	− 5122.960
		αYZ	− 15.629	βXXZ	− 225.335
		αZZ	213.700	βXYZ	− 178.859
		α_{Total}	6.412×10^{-23}	βXZZ	− 103.695
		Δα	4.851×10^{-23}	βYZZ	− 131.075
				βZZZ	− 51.993
				βX	− 825.714
				βY	− 5442.214
				βZ	19.588
				β_{Total}	7.289×10^{-30}

Fig. 4 Density of states of the studied compound computed using Multiwfn software
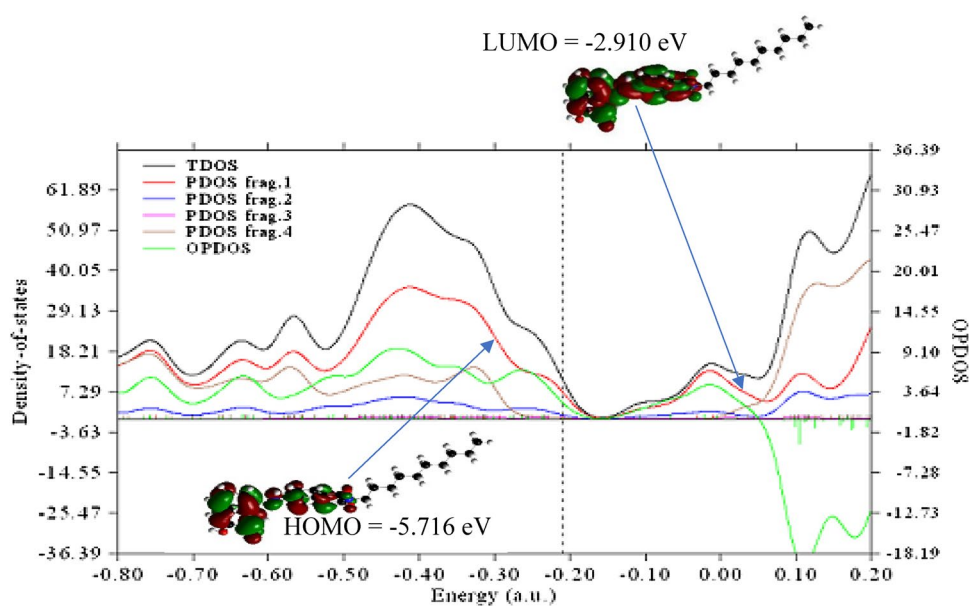
on the PDOS and OPDOS curves [36]. To determine the relative contributions of each atomic component, the AGI is divided into four atomic fragments as can be seen in Fig. 4. The contributions of fragments 1, 2, 3, and 4 are indicated by the colors (red, blue, magenta, and purple) for carbon, hydrogen, oxygen, and nitrogen atoms, respectively.

The discrete vertical lines signify molecular orbital and the dashed lines represent the highest occupied molecular orbital (HOMO). From the graph, the highest contribution was made by carbon (fragment 1) with red curve as seen in the HOMO. Howbeit, the positive OPDOS value between 3.64 and 9.10 a.u (green curve) which corresponds to bonding between fragments 1 and 4 (red and purple curve),

suggests that carbon is important for the stabilization of nitrogen atoms. Fragment 3, (magenta curve) gave little or no contribution to the HOMO–LUMO. This could be attributed to the − I effects of oxygen atom though its contribution was sparingly made to the molecular orbital between − 0.50 to − 0.30 a.u. Finally, the negative value of OPDOS at − 1.82 to − 18.19 a.u region implies antibonding characteristics between fragment 1 and 2 which is due to the unfavorable overlapping in the orbital phase. It could therefore be concluded that the major contributions made by carbon and nitrogen atoms to the HOMO–LUMO is as a result of the clouded electron density on carbon and nitrogen atoms used for interaction.

Table 8 Physicochemical properties of the investigated compound

Molecular weight	525.65
Hydrogen bond acceptors	6
Hydrogen bond donors	2
No of rotatable bonds	11
TPSA	102.56
LogP$_{O/W}$	4.97
Lipinski's violation	1

3.7 In Silico Assessment of ADMET Properties

The synthesized compound was analyzed for its drug—likeness, pharmacokinetics and medicinal chemistry friendliness using Swiss ADME [37]. The ADMET properties results obtained as shown in Tables 8 and 9 were evaluated with respect to the Lipinski's rule of 5 (RO5) [38].

The examined molecule only breaks one of Lipinski's rules, it can be regarded as orally bioavailable (molecular mass greater than 500, bioavailability score: 0.55). The ADMET result in Table 9 also demonstrated a superb human intestine absorption value of 97.28%, indicating that the drug under study had sufficient cell membrane permeability and bioavailability. Considering a key prerequisite for an oral drug's observed effectiveness is human intestine absorption. The target substance likewise had a poor value for skin permeability of −5.09 cm/s. This is a crucial element to take into account when using transdermal drug administration since it affects the medication's effectiveness. Another pharmacokinetic measure is the blood–brain barrier's permeability. We also examined how well a chemical inhibited CYP (cytochrome P450) and P-gp (permeability glycoprotein) enzymes (table S6 of the supporting information). Since the substance hasn't been proved to cross the blood–brain barrier, adverse effects on the central nervous system are prevented [39] Along with the CYPs, the P-gp is an important participant in the excretion processes and plays a crucial role in the process of an active efflux across biological membranes. The substance under investigation

Table 9 ADMET properties of AGI

Absorption	Water solubility	−3.133	Numeric (log mol/L)
	CaCO$_2$ permeability	0.04	Numeric (log Papp in 10^{-6} cm/s
	Human intestinal absorption	97.283	Numeric (% absorbed)
	Skin permeability	−2.735	Numeric (log Kp)
	P-glycoprotein substrate	Yes	Categorical (yes/no)
	P-glycoprotein I inhibitor	Yes	Categorical (yes/no)
	P-glycoprotein II inhibitor	Yes	Categorical (yes/no)
Distribution			
	VDss (human)	−1.521	Numeric (log L/kg)
	Fraction unbound (human)	0.045	Numeric (Fu)
	BBB permeability	−1.327	Numeric (log BB)
	CNS permeability	−1.986	Numeric (log PS)
Metabolism			
	CYP3A4 substrate	Yes	Categorical (yes/no)
	CYP2C19 inhibitor	Yes	Categorical (yes/no)
	Inhibitor	Yes	Categorical (yes/no)
Excretion			
	Total clearance	−0.307	Numeric (log ml/min/kg)
	Renal OCT2 substrate	No	Categorical (yes/no)
Toxicity			
	AMES toxicity	No	Categorical (yes/no)
	Max tolerated dose (human)	0.293	Numeric (log mg/kg/day)
	hERG I inhibitor	No	Categorical (yes/no)
	hERG II inhibitor	Yes	Categorical (yes/no)
	Oral Rat Acute Toxicity (LD50)	2.531	Numeric (mol/kg)
	Oral Rat Chronic Toxicity (LOAEL)	2.264	Numeric (logmg/kg_bw/day)
	Hepatotoxicity	Yes	Categorical (yes/no)
	Skin sensitisation	No	Categorical (yes/no)
	T.Pyriformis toxicity	0.285	Numeric (log ug/L)
	Minnow toxicity	−3.506	Numeric (log mM)

is a P-gp substrate. Additionally, the substance does not exhibit any CYP inhibition. The substance does not inhibit (CYP1AZ, CYP2C19, CYP2C9, CYP2D6, and CYP3A4) enzymes. A biological test to evaluate the mutagenesis potential of chemical substances is the AMES toxicity, **AGI** has no AMES toxicity. AGI has no skin sensitivity, which implies that it is safe and unable to produce allergies on the skin. Its Maximum Tolerated Dose (MTO) in humans is 0.293. The lipophilicity property Logp < 5 is fundamental for the success in drug development [40]. The synthesized compound possessed good drug likeness, as well as ADMET properties thus, can be viewed as a good material for drug development.

3.8 Molecular Docking Analysis

Molecular docking is one of the most used virtual screening techniques in finding active molecules from already-existing chemicals in a quest to identify and develop new drugs. The capacity of molecular docking to predict the structure, as well as the binding affinities of ligand and protein, is helpful information for drug development [41]. Molegro virtual docker [42], AutoDock Vina 4.1 and discovery studio 2021[43] were used to study the interaction between studied compound and of the breast cancer protein receptors PR (20VM), MTOR(4JT6), P13Kα(5T7F), Her-α(5T1Z) and EGFR(4R5Y).and the compound of interest. The target proteins' crystalline structures were downloaded in PDB format from the protein data bank. The proteins and ligand were prepared and docked using molegro virtual docker software and Autodock Vina respectively while the docked results were visualized and analyzed using Biovia discovery studio 2020. The docked results showed the interactions of the ligand with the selected receptor proteins associated with breast cancer. 4JT6 is a mammalian target of rapamycin (mTOR), 2OVM is a Selective progesterone receptor (SPR) [44], a phosphoinositide 3-kinase-related protein kinase, whose active site is highly recessed owing to the FKBP12–rapamycin-binding (FRB) domain and an inhibitory helix protruding from the catalytic cleft, that regulates cell proliferation in response to nutrients and growth factors, which is often denationalized in cancer [45]. 4R5Y is a B-RAF, is a member of the RAF kinase group, has been identified as a target for cancer therapy [46]. 5T1F is an Estrogen receptor (ERα), which when Complexed with the inhibitor can result in apoptosis in Breast Cancer [47]. The critical outcome of a survival pathway, that make up the human genome, is to ensure the sustenance of normal cells proliferation via Estrogen-induced apoptosis. 5T7F is a PI3Kdelta transferase and are also targeted by inhibitors in cancer treatment [47]. The lower the binding affinity, the stronger the ligand–protein interactions.

Table 10 Binding affinities of ligands (AGI and ARO) with receptor proteins

	AGI (kcal/mol)	ARO (kcal/mol)
2OVM	− 6.20	− 8.00
4JT6	− 8.10	− 9.80
4R5Y	− 9.90	− 10.10
5T1Z	− 6.50	− 6.90
5T7F	− 8.50	− 8.80
Mean binding affinity	− 7.84	− 8.72

T test of difference = 0 (vs ≠): T value = 1.20 P value = 0.261 DF = 9

(p value > α: the difference between the mean is not statistically significant

Table 10 depicts the binding affinity of **AGI** and the reference drug (Aromasin).

Figure 5 shows the 3-D representation of the Ligands (**AGI** and ARO), Also Figure S10 of the supporting information show the 2-D representation of Ligands (**AGI** and ARO) and amino acids interactions and Table 10 shows the average binding affinity based on the method established in previous study. The ligand **(AGI)** was compared with Aromasin (ARO), a standard agent for breast cancer management (ARO) to compare it to the compound under investigation. With **2OVM**, **AGI** indicated a binding affinity of − 6.2 kcal/mol due to dual conventional hydrogen bond (H-bond) with A: ARG:40 and A: SER:733 at 4.77 and 4.41 Å. Other hydrophobic interactions observed include Pi-sigma with A:VA:730 at 5.64 Å, Pi-Pi Stacked with A: TRP:755 at 6.25 Å, Pi-Alkyl and Alkyl with A: ILE:748 at 4.11 Å, A: ILE:751 at 7.01 Å and A: LEU:726 at 5.70 Å, A: TRP:5.85 at 5.86 Å. **4JT6** indicates a binding affinity of − 8.1 kcal/mol with AG1, due to a single H-bond with A: GLY:1897 at distance of 2.56 Å, and carbon–hydrogen bond (C–H-bond) with A: GLN:1937 and A: ALA:1971 at distances of 3.23 and 3.37 Å, the other are hydrophobic interactions of pi-alkyl and alkyl with A: LEU:1900, A:PRO:1975, A: ILE:2228, and A:PRO:1940 at distances > 4.00 Å. **4R5Y** interaction with AG1 indicates a binding affinity of − 9.9 kcal/mol due to a single H-bond a distance of 2.68 Å with A:LYS:483 but indicates multiple hydrophobic interaction; Pi-sigma with A:VAL:471, pi-pi- T-shaped and Stacked with A:TRP:531 and A:PHe:583, Pi-Alkyl and Alkyl with A:LEU:567, A:ILE:513, A:HIS:574, A:ILE:592, A:LEU:505, A:LEU:514, A:ALA:481 and A:ILE:463, all at distance > 4.00 Å. **5T1Z** interaction with AG1 indicates a binding affinity of − 6.5 kcal/mol, but did not showed any H-bond and this is based on interaction that are all hydrophobic, which include pi-sigma with A:ILE:358 and A:LEU:539 at distances of 3.56, 3.95, 4.88 and 3.94 Å, pi-alkyl and alkyl with A:LEU:379, A:VAL:376, A:MET:543, and A:LEU:362 at distances of > 3.90 Å. The binding affinity of − 7.84 kcal/

AGI

ARO

2ovm

4jt6

4r5y

5t1z

Fig. 5 3D Representations of the interaction between the studied ligand and the receptor proteins
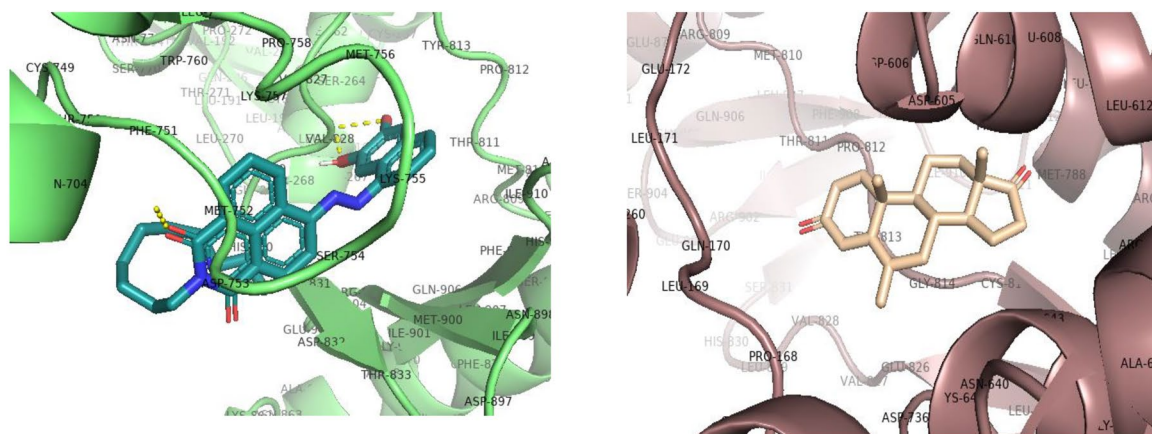
5t7f

Fig. 5 (continued)

mol was observed for **5T7F** interaction with AG1, due to two H-bond with A: LYS:708 and A: VAL:828 at distances of 2.80 and 1.99 Å, and additional strong electronic attraction due to pi-sulphur with A: MET:752 at distances of 4.09 and 3.90 Å. Also, pi-sigma was observed with A: ILE:910 at 3.66 Å, pi–pi T-shaped with A: TRP:760 and A: TYR:813 at 5.01, 5.30 and 5.41 Å, and lastly, pi-alkyl with A: ILE:825, A: ILE:777, A: MET:900 and A: MET:752 at distances > 4.00 Å. AG1 has a mean binding affinity of − 7.84, that ranges from − 6.2 to − 9.9 kcal/mol across all the receptor proteins under consideration, with the highest being − 9.9 kcal/mol for 4R5Y, followed by − 8.5 for 5T7F, − 8.1 for 4JT6, − 6.5 for 5T1Z for and − 6.2 kcal/mol for 2OVM. ARO shows reactivity and selectivity only with 2OVM with a binding affinity of − 8.0 kcal/mol was indicated on two H-bond with A: ARG:740 at 2.36 Å and A: GLN:747 at 2.50 Å. But with the other receptor proteins, no interactions were observed with the amino acid residues, indicating non-selectivity but reactivity with binding affinities of − 9.8 with 4JT6, − 10.1 with 4R5Y, − 6.9 with 5T1Z and 5T7F with − 8.8 kcal/mol. non-selectivity is an undesired phenomenon in drugs action as it does not allow for the exact mechanism and pathway of the drug metabolism and efficiency to be established. Therefore, AG1 has shown both excellent selectivity and reactivity when compared to ARO with average reactivity that is higher than AG1 but was not statistically significant, but AG1 has a defined selectivity in addition to the recorded reactivity. Due to the observed interaction of 2OVM and **AGI**, **AGI** is a selective progesterone receptor modulator (SPRMs) and is a potential clinical agent for the management of reproductive maladies. Conclusively, **AGI** exhibited antagonism, but not agonism, in a PR-B transfection assay and the T47D breast cancer cell alkaline phosphatase activity assay which is similar to findings with Madauss et al. [48]. The mTOR together with activating mutations, points to substrate recruitment

as a major mechanism controlling the kinase activity [49]. The FRB acts as a gatekeeper, that recruits S6K1 to restrict access to the active site, while also granting privileged substrates access through its binding site for the secondary motif. Therefore, **AGI** have privilege access, while ARO was denied access to the active site which support the molecular docking outcome with 4JT6 mTOR receptor protein. With 4R5Y, **AGI** is a B-RAF inhibitor with the potential to inhibit both BRAF V600E and EGFR drives RAF activation, which consequently provides a therapeutic benefit in the management of B-RAF mutated cancer. With 5T1Z, **AGI** inhibits estrogen by alteration of the conformation of the ER complexes, with changes in coactivator binding, governs estrogen-induced apoptosis through the PERK sensor system to trigger an Unfolded Protein Response (UPR) [50].

The result indicates that **AGI** is a potential therapeutic agent for the management of malignant breast cancer due to its reactivity and selectivity with relevant receptor proteins when juxtaposed with ARO and provides a platform for future clinical trials and possible drug development.

3.9 Statistical Analysis

The results obtained for the binding affinity between the AG1 and ARO was evaluated for the significant difference using a two-sample T test at a confidence interval of 95% using the minitab17 statistical software, the difference between the mean is not statistically significant.

4 Conclusion

(E)-2-decyl-6-((6,7-dihydroxynaphthalen-1-yl)diazinyl)-1H-[de] isoquinoline-1,3(2H)-dione (**AGI**) was synthesized and characterized using the various spectroscopic techniques like ^{1}HNMR, FTIR, and UV–Vis spectroscopy,

the result obtained show good agreement between the theory and experimental. The HOMO–LUMO energy gap which corresponds to the difference between HOMO and LUMO energies of the studied compound is theoretically found to be 2.806 eV, this, indicates the presence of NLO effect, low kinetic stability and high biological activity of the studied compound. The various atomic charge analysis carried out show that the heteroatoms (O, N) contributed greatly to the reactivity and stability of the studied compound, this result was further confirmed by natural bond orbital (NBO) analysis result as seen in the high value of energy of stabilization (67.03, 37.46) Kcal/mol for (LP (1) N18/πC17–O20 and LP (2) O69/πC57–C61) interactions respectively. The molecular docking result suggests that AG1 is a potential therapeutic agent for the management of malignant breast cancer due to its reactivity and selectivity with relevant receptor proteins when juxtaposed with **Aromasin** and provides a platform for future clinical trials and possible drug development. ADMET analysis also showed good drug likeness and excellent ADME properties as well as permissible toxicity assessment. Hence, this present study will provide a useful guide for further studies and synthesis of (E)-2-decyl-6-((6,7-dihydroxynaphthalen-1-yl)diazinyl)-1H-[de] isoquinoline-1,3(2H)-dione which may evolve an anticancer agent in the future.

Declarations

Conflict of interest There are no conflicts to declare.

References

1. Roco Á, Cerda B, Cayún JP, Lavanderos A, Rubilar JC, Cerro R et al (2018) Pharmacogenetics, tobacco, alcohol and its effect on the risk development cancer. Revista Chilena de Pediatria 89(4):432–440
2. Raguz S, Yagüe E (2008) Resistance to chemotherapy: new treatments and novel insights into an old problem. Br J Cancer 99(3):387–391
3. Sreejaya SB, Santhy KS (2013) Cytotoxic properties of Acorus calamus in MCF-7 breast cancer cells. Int J Curr Res Acad Rev 1(1):106–111
4. Aiello S, Wells G, Stone EL, Kadri H, Bazzi R, Bell DR et al (2008) Synthesis and biological properties of benzothiazole, benzoxazole, and chromen-4-one analogues of the potent anti-tumor agent 2-(3, 4-dimethoxyphenyl)-5-fluorobenzothiazole (PMX 610, NSC 721648). J Med Chem 51(16):5135–5139
5. Rehman N, Khalid M, Bhatti MH, Yunus U, Braga AAC, Ahmed F et al (2018) Schiff base of isoniazid and ketoprofen: synthesis, X-ray crystallographic, spectroscopic, antioxidant, and computational studies. Turk J Chem 42(3):639–651
6. Odey JO, Louis H, Agwupuye JA, Moshood YL, Bisong EA, Brown OI (2021) Experimental and theoretical studies of the electrochemical properties of mono azo dyes derived from 2-nitroso-1-naphthol, 1-nitroso-2-naphthol, and CI disperse yellow 56 commercial dye in dye-sensitized solar cell. J Mol Struct 1241:130615
7. Doloczki S, Holmberg KO, Galván IF, Swartling FJ, Dyrager C (2022) Photophysical characterization and fluorescence cell imaging applications of 4-N-substituted benzothiadiazoles. RSC Adv 12(23):14544–14550
8. Eno EA, Louis H, Unimuke TO, Agwamba EC, Etim AT, Mbonu JI et al (2022) Photovoltaic properties of novel reactive azobenzo-quinolines: experimental and theoretical investigations. Phys Sci Rev. https://doi.org/10.1515/psr-2021-0191
9. Frisch MJ, Trucks GW, Schlegel HB, Scuseria GE, Robb MA, Cheeseman JR, Scalmani G, Barone V, Petersson GA, Nakatsuji H, Li X, Caricato M, Marenich AV, Bloino J, Janesko BG, Gomperts R, Mennucci B, Hratchian HP, Ortiz JV, Izmaylov AF, Sonnenberg JL, Williams-Young D, Ding F, Lipparini F, Egidi F, Goings J, Peng B, Petrone A, Henderson T, Ranasinghe D, Zakrzewski VG, Gao J, Rega N, Zheng G, Liang W, Hada M, Ehara M, Toyota K, Fukuda R, Hasegawa J, Ishida M, Nakajima T, Honda Y, Kitao O, Nakai H, Vreven T, Throssell K, Montgomery Jr JA, Peralta JE, Ogliaro F, Bearpark MJ, Heyd JJ, Brothers EN, Kudin KN, Staroverov VN, Keith TA, Kobayashi R, Normand J, Raghavachari K, Rendell AP, Burant JC, Iyengar SS, Tomasi J, Cossi M, Millam JM, Klene M, Adamo C, Cammi R, Ochterski JW, Martin RL, Morokuma K, Farkas O, Foresman JB, Fox DJ (2016) Gaussian, Inc., Wallingford
10. Dennington R, Keith TA, Millam JM (2016) GaussView 6.0. 16. Semichem Inc.: Shawnee Mission, KS, USA. HyperChem, T. (2001). HyperChem 8.07, HyperChem Professional Program. Gainesville, Hypercube
11. Jomroz MH (2004) Vibrational energy distribution analysis, VEDA4. ScienceOpen Inc., Warsaw
12. Lu T, Chen F (2012) Multiwfn: a multifunctional wavefunction analyzer. J Comput Chem 33(5):580–592
13. Kazarian SG, Chan KLA (2006) Applications of ATR-FTIR spectroscopic imaging to biomedical samples. Biochimica et Biophysica Acta (BBA) Biomembranes 1758(7):858–867
14. Gunasekaran S, Seshadri S, Muthu S, Kumaresan S, Arunbalaji R (2008) Vibrational spectroscopy investigation using ab initio and density functional theory on *p*-anisaldehyde. Spectrochimica Acta Part A Mol Biomol Spectrosc 70(3):550–556
15. Mumit MA, Pal TK, Alam MA, Islam MAAAA, Paul S, Sheikh MC (2020) DFT studies on vibrational and electronic spectra, HOMO–LUMO, MEP, HOMA, NBO and molecular docking analysis of benzyl-3-*N*-(2,4,5-trimethoxyphenylmethylene) hydrazinecarbodithioate. J Mol Struct 1220:128715
16. Gunasekaran S, Seshadri S, Muthu S (2006) Vibrational spectra and normal coordinate analysis of flucytosine
17. Edim MM, Louis H, Bisong EA, Chioma AG, Enudi OC, Unimuke TO et al (2021) Electronic structure theory study of the reactivity and structural molecular properties of halo-substituted (F, Cl, Br) and heteroatom (N, O, S) doped cyclobutane. Phys Sci Rev. https://doi.org/10.1515/psr-2020-0138
18. Ayyappan S, Sundaraganesan N, Aroulmoji V, Murano E, Sebastian S (2010) Molecular structure, vibrational spectra and DFT molecular orbital calculations (TD-DFT and NMR) of the

antiproliferative drug methotrexate. Spectrochim Acta Part A Mol Biomol Spectrosc 77(1):264–275

19. Chandana SN, Al-Ostoot FH, Mohammed YHE, Al-Ramadneh TN, Akhileshwari P, Khanum SA et al (2021) Synthesis, structural characterization, and DFT studies of anti-cancer drug *N*-(2-aminophenyl)-2-(4-bromophenoxy) acetamide. Heliyon 7(3):e06464

20. Ameuru US, Okah PK, Saliu HR, Yakubu CI (2020) Synthesis and dyeing performance of azo-anthraquinone dyes on polyester fabrics. In: Science forum (Journal of Pure and Applied Sciences), vol 20, no 2. Faculty of Science, Abubakar Tafawa Balewa University Bauchi, pp 150–156

21. Ren Y, Li MY, Song YX, Sui MY, Sun GY, Qu XC et al (2021) Refined standards for simulating UV–Vis absorption spectra of acceptors in organic solar cells by TD-DFT. J Photochem Photobiol, A 407:113087

22. Prabakaran A, Vijayakumar V, Radhakrishnan N, Chidambaram R, Muthu S (2022) Experimental and quantum chemical computational analysis of novel N4,N4′-dimethyl-[1,1′-biphenyl]-3,3′,4,4′-tetraamine. Polycyclic Aromat Compd 42(3):925–941

23. ElKhattabi S, Hachi M, Fitri A, Benjelloun AT, Benzakour M, Mcharfi M, Bouachrine M (2019) Theoretical study of the effects of modifying the structures of organic dyes based on *N,N*-alkylamine on their efficiencies as DSSC sensitizers. J Mol Model 25(1):9

24. Bhavani K, Renuga S, Muthu S (2015) Quantum mechanical study and spectroscopic (FT-IR, FT-Raman, 13C, 1H) study, first order hyperpolarizability, NBO analysis, HOMO and LUMO analysis of 2-acetoxybenzoic acid by density functional methods. Spectrochim Acta Part A Mol Biomol Spectrosc 136:1260–1268

25. Ranjan P, Kumar P, Chakraborty T, Sharma M, Sharma S (2020) A study of structure and electronic properties of chalcopyrites semiconductor invoking Density Functional Theory. Mater Chem Phys 241:122346

26. Louis H, Gber TE, Asogwa FC, Eno EA, Unimuke TO, Bassey VM, Ita BI (2022) Understanding the lithiation mechanisms of pyrenetetrone-based carbonyl compound as cathode material for lithium-ion battery: insight from first principle density functional theory. Mater Chem Phys 278:125518

27. Undiandeye UJ, Louis H, Gber TE, Egemonye TC, Agwamba EC, Undiandeye IA, Adeyinka AS, Ita BI (2022) Spectroscopic, conformational analysis, structural benchmarking, excited state dynamics, and the photovoltaic properties of Enalapril and Lisinopril. J Indian Chem Soc 99(7):100500

28. Bassey VM, Apebende CG, Idante PS, Louis H, Emori W, Cheng CR et al (2022) Vibrational characterization and molecular electronic investigations of 2-acetyl-5-methylfuran using FT-IR, FT-Raman, UV–VIS, NMR, and DFT methods. J Fluoresc 32(3):1005–1017

29. Christopher JC (2004) Essentials of computational chemistry: theories and models

30. Mao JX (2014) Atomic charges in molecules: a classical concept in modern computational chemistry. J Postdr Res 2(2). https://doi.org/10.14304/SURYA.JPR.V2N2.2

31. Obu QS, Louis H, Odey JO, Eko IJ, Abdullahi S, Ntui TN, Offiong OE (2021) Synthesis, spectra (FT-IR, NMR) investigations, DFT study, in silico ADMET and molecular docking analysis of 2-amino-4-(4-aminophenyl) thiophene-3-carbonitrile as a potential anti-tubercular agent. J Mol Struct 1244:130880

32. Kores JJ, Danish IA, Sasitha T, Stuart JG, Pushpam EJ, Jebaraj JW (2021) Spectral, NBO, NLO, NCI, aromaticity and charge transfer analyses of anthracene-9,10-dicarboxaldehyde by DFT. Heliyon 7(11):e08377

33. Suresh M, Bahadur SA, Athimoolam S (2015) Investigations on spectroscopic, optical, thermal and dielectric properties of a new NLO material: l-histidinium *p*-toluenesulfonate [LHPT]. Optik 126(24):5452–5455

34. Asogwa FC, Agwamba EC, Louis H, Muozie MC, Benjamin I, Gber TE et al (2022) Structural benchmarking, density functional theory simulation, spectroscopic investigation and molecular docking of *N*-(1H-pyrrol-2-yl) methylene)-4-methylaniline as castration-resistant prostate cancer chemotherapeutic agent. Chem Phys Impact 5:100091

35. Nicholson MIG, Bueno PR, Feliciano GT (2020) Ab initio QM/MM simulation of ferrocene homogeneous electron-transfer reaction. J Phys Chem A 125(1):25–33

36. Sadeghi S, Shiri HM, Ehsani A, Oftadeh M (2020) Electrosynthesis of high-purity TbMn$_2$O$_5$ nanoparticles and its nanocomposite with conjugated polymer: surface, density of state and electrochemical investigation. Solid State Sci 105:106227

37. Eno EA, Louis H, Unimuke TO, Gber TE, Mbonu IJ, Ndubisi CJ, Adalikwu SA (2022) Reactivity, stability, and thermodynamics of para-methylpyridinium-based ionic liquids: insight from DFT, NCI, and QTAIM. J Ion Liq 2(1):100030

38. Lipinski CA, Lombardo F, Dominy BW, Feeney PJ (1997) Experimental and computational approaches to estimate solubility and permeability in drug discovery and development settings. Adv Drug Deliv Rev 23(1–3):3–25

39. Leo A, Hansch C, Elkins D (1971) Partition coefficients and their uses. Chem Rev 71(6):525–616

40. Eno EA, Mbonu JI, Louis H, Patrick-Inezi FS, Gber TE, Unimuke TO et al (2022) Antimicrobial activities of 1-phenyl-3-methyl-4-trichloroacetyl-pyrazolone: experimental, DFT studies, and molecular docking investigation. J Indian Chem Soc 99(7):100524

41. Egemonye TC, Louis H, Unimuke TO, Gber TE, Edet HO, Bassey VM, Adeyinka AS (2022) First principle density functional theory study on the electrochemical properties of cyclohexanone derivatives as organic carbonyl-based cathode material for lithium-ion batteries. Arab J Chem 15(23):104026

42. Bitencourt-Ferreira G, Azevedo WFD (2019) Molegro virtual docker for docking. In: Docking screens for drug discovery. Humana, New York, pp 149–167

43. Biovia DS, DSME R (2017) San Diego: Dassault Systèmes, 2016

44. Tang Z, Yuan X, Du R, Cheung S, Zhang G, Wei J (2015) BGB-283, a novel RAF kinase and EGFR inhibitor, displays potent antitumor activity in B-RAF mutated colorectal cancers. Am Assoc Cancer Res. https://doi.org/10.1158/1535-7163.MCT-15-0262

45. Benjamin I, Udoikono AD, Louis H, Agwamba EC, Unimuke TO, Owen AE, Adeyinka AS (2022) Antimalarial potential of naphthalene-sulfonic acid derivatives: molecular electronic properties, vibrational assignments, and in-silico molecular docking studies. J Mol Struct 1264:133298

46. Patrick-Inezi FS, Emori W, Louis H, Apebende CG, Agwamba EC, Unimuke TO et al (2022) Analeptic activity of 2-hydroxy-5-nitrobenzaldehyde: experimental, DFT studies, and in silico molecular docking approach. Healthc Anal 2:100030

47. Yang H, Rudge DG, Koos JD, Vaidialingam B, Yang HJ, Pavletich NP (2013) mTOR kinase structure, mechanism and regulation. Nature 497(7448):217–223

48. Agwamba EC, Udoikono AD, Louis H, Udoh EU, Benjamin I, Igbalagh AT et al (2022) Synthesis, characterization, DFT studies, and molecular modeling of azo dye derivatives as potential candidate for trypanosomiasis treatment. Chem Phys Impact 4:100076

49. Agwamba EC, Hassan LG, Muhammad A, Sokoto AM (2019) Taguchi optimization of carboxymethylation process and effect reaction efficiency on swelling capacity. Asian J Appl Sci 7(5). https://doi.org/10.24203/ajas.v7i5.5954

50. Osigbemhe IG et al (2022) Synthesis, characterization, DFT studies, and molecular modeling of 2-(-(2-hydroxy-5-methoxyphenyl)-methylidene)-amino) nicotinic acid against some selected bacterial receptors. J Iran Chem Soc 19:3561–3576